Morphology and Conductivity of Copper Hexacyanoferrate Films

Pouya Hosseini, Konrad Wolkersdörfer, Michael Wark, Engelbert Redel, Helmut Baumgart, and Gunther Wittstock*

ABSTRACT: Films of conductive coordination network com pounds are interesting as functional materials for charge storage, electrocatalysis, electrochromic switching, or conversion of light. The electrical conductivity depends on not only intrinsic material properties but also grain boundaries. Copper hexacyanoferrate shows a remarkable variation in film morphologies depending on the preparation route. Conductive films can only be obtained for continuous crystalline films that have been received by a combination of sonication assisted casting and vapor assisted conversion. Electrical conductivities of these films are higher than those of powder pellets with a similar crystal structure. Temper ature dependent and humidity dependent measurements on powder pellets revealed the activation energies for charge transport. Thermogravimetric analysis, temperature dependent X ray diffrac tion data, and humidity dependent measurements on powder pellets revealed the activation energies for charge transport and the role of proton conductivity.

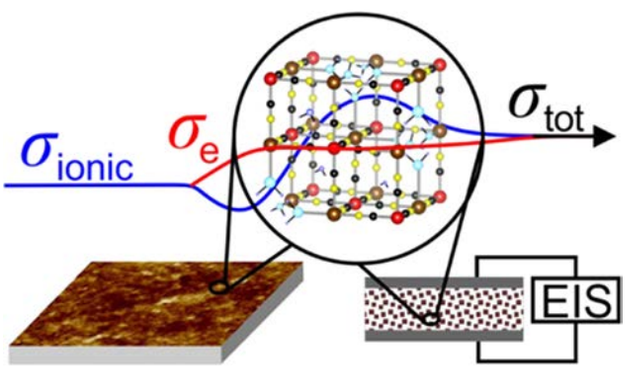

INTRODUCTION

Metal hexacyanometalates (MHCMs) form a large family of coordination network compounds,[1−3] among which Prussian blue (PB) is probably the best known representative.[4−6] Due to the redox transition of the coordinated transition metal ions, mixed valence states are accessible.[7] The charge associated with the valence change of the transition metal ions is compensated by uptake/ejection of alkali metal ions from/into the coordination network formed by the transition metal ions and the bridging cyanide ligands. Over the past two decades, an extensive variety of these compounds have been synthesized with the general formula $A_xM[M'(CN)_6]_z{\cdot}nH_2O$ (N coordinated M = Fe, Cu, Ni, Co, Ti, Zn, In, Ga, Cd, Cr, Pb, Mn, Al, Ga, Ag; C coordinated M′ = Fe, Ru, Os, Rh, Mn, Cr, Ti, Ir, V, Co; A = alkali metal cation or NH_4^+).[8−10] The exceptional variety and tunability of their physical and chemical properties are due to the three dimensional frame work of alternating metal knots connected by a noninnocent small bridging ligand forming interconnected channels that can accommodate solvent molecules and counterions.[11] Therefore, these materials have been comprehensively studied in several different fields, including electrochemistry,[12,13] electrocata lysts,[14] electrochemical sensors,[15,16] switchable sorption materials,[17−19] electrochromic windows,[2,20,21] and charge storage devices.[2,22−26] This interest has recently been revived also in view of the high natural abundance of the constituting elements. For the mentioned applications, conductivity is critical,[27−29] to which (i) band conductivity by mobile electrons or holes (electronic conductivity),[30−32] (ii) electron hopping in mixed valence states, (iii) ionic conductivity by mobile alkali ions in the channels of the MHCMs,[33] and (iv) proton conductivity[34−36] may contribute. Proton conductivity is enabled by Grotthuss conduction mechanisms because water is typically present in MHCMs either as coordinated to a transition metal ion (replacing CN^- at regular or defect positions) or enclosed in the channel structure (zeolitic water).[34,36] Here, we explore the suitability of using MHCMs as alternative semiconducting electronic materials that enable switching behavior through modification of the redox state. To exploit conductivity, the materials must be prepared as conductive films with macroscopic extensions that connect external current collectors (or contact pads) without the use of a conductive additive.[37]

Despite an abundance of constituting elements and a (seemingly) simple synthesis, the preparation of these materials with defined structural and functional properties is challenging. At the level of the crystal structure, many MHCMs occur in at least two forms,[39,40] which are shown for copper hexacyanoferrate (CuHCF, $K_{2x/3}Cu^{II}[Fe^{III}(CN)_6]_{2/3}{\cdot}nH_2O$) in

Scheme 1. Synthesizing only one of them requires substantial effort and is typically incompatible with the production of

Scheme 1. Structures of $KCu^{II}[Fe^{III}(CN)_6]$ and $Cu^{II}[Fe^{III}(CN)_6]_{2/3}{\cdot}nH_2O$[a]

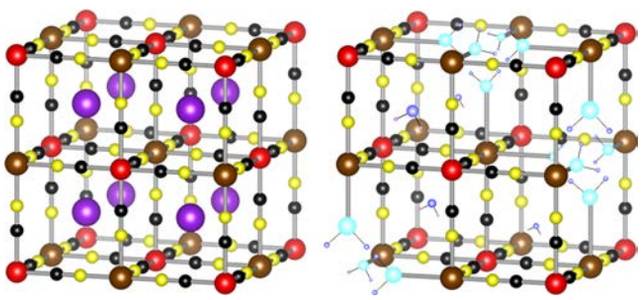

[a]Color code for $Cu^{II}[Fe^{III}(CN)_6]_{2/3}{\cdot}nH_2O$: red, Fe; brown, Cu; black, C; yellow, N; violet, K; O atoms of coordinated water are shown in cyan and those of zeolitic water in blue. The schematic was created with VESTA 3[38] and data from ref 39.

films. Often, motifs of one of the structures in Scheme 1 occur as "defects" in the dominating alternative form. Therefore, the precise characterization of the material is often challenging even when using a wide variety of structural characterization methods, such as infrared (IR) spectroscopy,[41,42] X ray absorption spectroscopy,[43,44] X ray diffraction (XRD),[39,43] X ray photoelectron spectroscopy (XPS),[45,46] Mössbauer spectroscopy,[43] and thermogravimetric analysis (TGA).[43] The simultaneous occurrence of irregularities in the coordination environment of some transition metals and the variation in redox states create many possible structural motifs of similar energy, especially when the film is in contact with an electrolyte and exposed to changing potentials—a typical scenario for several important applications. This was recently highlighted by an in operando infrared reflection−absorption spectroscopic study on cobalt hexacyanoferrate (CoHCF, $Co^{II}[Fe^{III}(CN)_6]_{2/3}{\cdot}nH_2O$) and CuHCF.[41] The large variety of structural features is further enriched when considering the film's growth on different substrate materials, which has not yet received the same attention as other properties of MHCMs.

Here, we present results on copper hexacyanoferrate (CuHCF, $K_{2x/3}Cu^{II}[Fe^{III}(CN)_6]_{2/3}{\cdot}nH_2O$), which demonstrate particularly well the variation in film morphology and its influence on conductivity as a key functional property. Density functional theory calculations predict for CuHCF one of the lowest ligand field splitting among the simple metal hexacyanoferrates,[28,47,48] which would favor the electronic conductivity of the material. We expected different influences on the conductivity of a macroscopic film that may originate from changes of the dominating conductance mechanisms because of the possible variations in their structures,[39] the number of defects, and the connection between different grains in a macroscopic film. The latter two may be largely influenced by the film preparation technique.

EXPERIMENTAL SECTION

Materials and Chemicals. 4′ Mercaptobiphenyl carbonitrile (≥97%, Sigma Aldrich), 3 cyanopropyltrichlorosilane (≥97%, Sigma Aldrich), $K_3[Fe(CN)_6]$ (≥99%, Alfa Aesar), $CuCl_2$ (≥98%, Merck Schuchardt), H_2SO_4 (97%, Sigma Aldrich), H_2O_2 (30%, VWR), ethanol (99.8%, Sigma Aldrich), acetone (≥99.5%, Sigma Aldrich), acetonitrile (≥99.5%, VWR), and gold wire (99.999%, GoodFellow) were used as received. Deionized water (ELGA LabWater, Celle, 18.2 MΩ cm at 296 K) was used to prepare solutions. Muscovite mica sheets were obtained from SPI Supplies (West Chester, PA), and p silicon wafers were from Silchem Handelsgeselschaft GmbH (Freiburg, Germany).

Electrodeposition. The CuHCF films in Figure 1 were electrodeposited at room temperature on a polycrystalline gold film electrode (on glass, Cr as an adhesion layer) by applying 20 potential cycles between 0.5 and 0.9 V at a scan rate ν = 0.05 V s^{-1} using a potentiostat (CH660A, CH Instruments, Austin, TX). The three electrode cell consisted of a gold film electrode as a working electrode (WE), a Pt foil as an auxiliary (Aux) electrode, and a Ag|AgCl|3 M KCl as a reference (Ref) electrode to which all potentials are referred to. The electrolyte solution contained 0.5 mM $K_3[Fe(CN)_6]$, 0.5 mM $CuCl_2$, and 0.5 M K_2SO_4 and was deoxygenated by purging with Ar for 30 min.

Layer-by-Layer (LbL) Fabrication of Thin Films of CuHCF. LbL deposition was carried out on cyanide terminated organic layers on either template stripped gold or thermally oxidized silicon wafers (SiO_x|Si) for the experiments in Figures 2 and 3. The preparation of these substrates is detailed in the Supporting Information (Section SI 1). The LbL deposition followed the procedure described before.[41] Briefly, the substrate was mounted on a frame at the end of a computer controlled homemade mechanical hand robot (operated by Robo Pro software; Fischer Technik, Waldachtal, Germany). The robot transferred the substrate in 30 cycles between the vials containing 0.15 M $CuCl_2$ in water (immersion time 20 min), water for rinsing, 0.125 M $K_3[Fe(CN)_6]$ in water (immersion time 20 min), and water for rinsing again.

Bulk Synthesis. $K_{2x/3}Cu^{II}[Fe^{III}(CN)_6]_{2/3}{\cdot}nH_2O$ was obtained by dropwise adding 50 mL of 0.25 M $K_3[Fe(CN)_6]$ to 100 mL of 0.30 M $CuCl_2$ in a glass jacketed reactor vessel over 1 h at 50 °C under an Ar atmosphere with constant stirring. It is necessary to add $K_3[Fe(CN)_6]$ gradually to $CuCl_2$ to maintain an excess of Cu(II) at each stage to form a potassium free product.[43,49] Afterward, the reaction mixture was aged for 4 h at 50 °C under Ar. The precipitates were separated from the mother liquid through centrifugation, washed several times with distilled water, and dried under Ar at 60 °C. This powder was used to prepare pellets of 8.2 mm diameter and 0.43 mm thickness for the experiments in Figures 6 and 7. The powder was compressed between two porous stainless steel electrodes by a torque of 40 cN m. A graphite felt (GDL 25 BC, SGL Carbon, Wiesbaden, Germany) ensured the electrical connection of the pellet and the current collectors.

CuHCF Film Fabrication by Sonication-Assisted Casting (SAC) and Vapor-Assisted Conversion (VAC). The synthesis of the bulk CuHCF was performed similar as described above but at lower temperature (in order to obtain smaller seeds) and with a different workup. It was used for the films in Figures 4 and 5. The synthesis of the bulk CuHCF was performed similarly to that described above but at a lower temperature (to obtain smaller seeds) and with a different workup. In detail, 50 mL of 0.25 M $K_3[Fe(CN)_6]$ was added to 100 mL of 0.30 M $CuCl_2$ in a glass jacketed reactor vessel over 1 h at 0 °C under an Ar atmosphere with constant stirring. Immediately afterward (i.e., without aging), the precipitates were separated from the mother liquid by centrifugation and washed several times with an ethanol−water mixture [50/50% (v/v)] to remove KCl. The solid product was then dispersed in

an ethanol–water mixture [50/50% (v/v)] as a colloidal dispersion with a suitable concentration for casting in the next step.

The material content of this stock suspension was calculated as c_{stock}, which provides the concentration of formula units ($K_{2x/3}Cu^{II}[Fe^{III}(CN)_6]_{2/3}\cdot 3.5H_2O$, x = 0.6 from XPS) per volume of the suspension. It is obtained from the molar mass M_{CuHCF} = 280.24 g mol^{-1} (with water) of one formula unit and the volume of the ethanol–water mixture used to prepare the dispersion. The substrate was placed on a piece of parafilm (R) (Pechiney Plastic Packaging, Menasha, WI) in a Petri dish. The Petri dish was floating in warm water (70 °C) inside an ultrasonic bath (Emmi 40HC, EMAG AG, Mörfelden Wall dorf, Germany). An aliquot of volume V_{stock} = 200 μL cm^{-2} of the dispersion was placed on the substrate with an area $A \approx 1$ cm^2 and allowed to dry while the substrate was sonicated (Figure 4a). This procedure yielded a continuous film with very low roughness. The thickness of the resulting film was estimated according to eq 1, where d is the film thickness and ρ_{CuHCF} = 1.83 g cm^{-3} is the density of CuHCF as calculated from XRD data and the water content of the bulk synthesized product.

$$d = \frac{c_{stock}\cdot V_{stock}\cdot M_{CuHCF}}{A\cdot \rho_{CuHCF}} \quad (1)$$

To improve the crystallinity of the film, the vapor assisted conversion (VAC) method was used (Figure 4b).[50−52] For this purpose, 15% (v/v) acetonitrile was added to a mixture of water/ethanol [50/50% (v/v)]. This solvent mixture was placed in a vial. The CuHCF coated substrates as obtained from SAC were placed above the solution. The reaction chamber was closed and placed in a temperature controlled water bath at 70 °C where the conversion was allowed to proceed for 3 h.

Characterization. *Cyclic Voltammetry.* Cyclic voltamme try in Figure 5 was performed at room temperature with a CH660A potentiostat in a three electrode cell with the CuHCF film electrode as the working electrode (A = 0.217 cm^2), a Pt foil as the auxiliary electrode, and an AglAgCll3 M KCl as the reference electrode to which all potentials are referred to. The electrolyte solution was deoxygenated by bubbling with Ar for 30 min. The 1 μm thick CuHCF film investigated in Figure 5 was prepared by the SAC–VAC method on a gold electrode.

X-ray photoelectron spectroscopy (XPS). XPS in Figures S2–S6 was performed with monochromatized Al Kα radiation. Further details are given in Section SI 2.

X-ray diffraction (XRD). The LbL film (Figure 3) and the film prepared by SAC–VAC (Figure 4e) were characterized using a Bruker D8 Advance equipped with a Si strip detector (PSD Lynxeye; position sensitive detector) with Cu K$\alpha_{1,2}$ radiation (λ = 0.15418 nm) in the θ–θ geometry and a variable slit on the primary circle. Data evaluation was performed with Eva software and data system (Bruker). Scans were run over various ranges with a step width of 0.024° 2θ and 84 s for higher order peaks up to 336 s per step. The 2θ angle scanning ranges to observe the corresponding peaks of the deposited film are from 16 to 36° (out of plane) and 7 to 41° (in plane).

XRD pattern of powders (Figures 6 and S11–S17) have been collected with a PANalytical X'pert PRO θ–θ X ray diffractometer (Malvern Panalytical B.V., Almelo, The Nether lands) operating at 40 kV and 40 mA. Measurements have been performed in the range of 10–70° 2θ with a step size of 0.0263° (2θ) and a counting time of 297 s. Powder samples have been prepared on a zero background silicon substrate and mounted on a reflection transmission spinner stage. The reaction chamber XRK900 (Malvern Panalytical) was applied for temperature dependent XRD. The temperature was controlled with a temperature control unit (TCU 750, Anton Paar GmbH, Graz, Austria). Patterns have been evaluated with software TOPAS Academic version 4.1.

Scanning Force Microscopy. Samples in Figures 1b, 2b,c, and 4d were measured with a scanning force microscope (SFM, Nanoscope IIIA controller and an Enviroscope stage, operated under Nanoscope Software V5.3r3s3, Veeco Instru ments Inc., Santa Barbara, CA) in the tapping mode with NCHV A tips (42 N m^{-1}, f_0 = 320 kHz, Bruker, Camarillo, CA).

Powder and Thick Film Conductometry. The conductivity of CuHCF in Figures 6a, S8, and S9 was determined by electrochemical impedance spectroscopy (EIS) on powder samples of pellets of 8.2 mm diameter and approx. 0.43 mm thickness compressed between two porous stainless steel electrodes by a torque of 40 cN m. A graphite felt (GDL 25 BC, SGL Carbon, Wiesbaden, Germany) ensures the electrical connection of the pellet and the current collector electrode. The sample holder from poly (tetrafluoro ethylene) was placed in a custom made cell[53] that was connected to the electro chemical work station (IM6e, Zahner, Kronach, Germany). The EIS spectra were recorded in the frequency range from 1 Hz to 1 MHz with an alternating voltage of 10 mV amplitude. The relative humidity was adjusted by means of the temperature difference between a temperature controlled sample chamber and a temperature controlled water reservoir, as described before.[54] Further details are provided in Section SI 3. The conductivity was extracted from the Bode plot at the frequency at which the phase angle reached its minimum.

One pellet prepared as described above was first characterized in a dry atmosphere at room temperature, then subjected to a VAC treatment, and measured again under identical conditions (Figure 8). To maintain the integrity of the sample, the entire EIS cell was placed in an autoclave filled with a solvent mixture of 15% (v/v) of acetonitrile in the water–ethanol mixture [50/50% (v/v)]. The reactor was placed in a water bath at 70 °C for 12 h. Inside the EIS cell, the powder pellet is sandwiched between the carbon felt and steel frits, which allow the exchange with the surrounding gas atmosphere and thus support the VAC process of the mounted powder pellet. To accommodate the larger thickness of the powder pellet and the restricted access to the sample in the EIS cell, the duration of SAC treatment was prolonged compared to the 1 μm thick film used for film conductivity measurements in Table 2.

Thin-Film Electrical Conductometry. Four contact van der Pauw samples were used for the thin film electrical conductivity measurements (Table 2), where corner contacts in square samples produce fewer errors than contacts placed at the center of the sample sides. These measurements were carried out with an Ecopia Hall effect measurement system (HMS 5300) equipped with 0.55 Tesla permanent magnet. We used a shadow mask to sputter the Au contacts through the mask openings to fabricate the four corner contacts. To ensure the integrity of the CuHCF films, we always used bottom Au contacts and synthesized the films on top of the predeposited gold contacts because a postfilm deposition sputter contact

process could affect the surface morphology of the CuHCF films. By utilizing van der Pauw samples, the electrical conductivity σ has been measured.

Thermogravimetric Analysis (TGA). TGA in Figure 7b,c was performed on a TGA 4000 (thermogravimetric analyzer, PerkinElmer, Inc., Waltham). A sample of 11.422 mg was equilibrated at 30 °C. The temperature was increased up to 350 °C at 10 K min^{-1} under an O_2 flow of 20 mL min^{-1}.

RESULTS AND DISCUSSION

Control of Film Morphology. *Electrodeposition.* The mechanism of electrochemical film deposition[55] starts with the reduction

$$[Fe^{III}(CN)_6]^{3-} + e^- = [Fe^{II}(CN)_6]^{4-} \quad (2)$$

followed by the precipitation with Cu^{2+} and K^+ on the electrode surface.

$$2K^+ + Cu^{2+} + [Fe^{II}(CN)_6]^{4-} = K_2Cu[Fe^{II}(CN)_6] \quad (3)$$

Other stoichiometries might be possible depending on the relative content of the structures in Scheme 1. Due to the lower reagent concentration, no spontaneous precipitation occurs in the solution. This process has the general advantage that the deposition can be site directed to electrodes, enabling the coating of microstructures and electrodes of complicated shape or even three dimensional architectures (Figure 1a).[56,57] A large variety of MHCMs have been electrodeposited on various electrode materials,[12] among them is CuHCF on glassy carbon.[58] Even epitaxial films have been obtained for FeHCFs on Au(110) single crystal electrodes.[59] However, contact mode SFM images in Figure 1b show that this procedure yields isolated deposits for CuHCF on Au. As demonstrated in our previous paper,[41] they exhibit a well defined electrochemical response despite the fact that no continuous film is formed and, therefore, no conductivity over macroscopic distances can be expected. As shown by in operando infrared reflection–absorption studies, a small fraction of the Cu(II) centers is oxidized to Cu(III) in the electrochemically deposited film.[41] The Cu(III) species are unstable and cause oxidation of Fe(II) to Fe(III). In addition, CuHCF shows "annealing," in which some cyanide groups change the coordination to C coordinated Cu ions and N coordinated Fe ions.[41]

Layer-by-Layer Deposition. In contrast to electrodeposition, LbL deposition on CN terminated organic layers (Figure 2a) on Au leads to films composed of well defined cubic crystals (Figure 2b). The film thickness can be exactly controlled by the number of LbL cycles. These films exhibit a well defined redox behavior in cyclic voltammetry.[41] This behavior is enabled by a mixed electronic and ionic conductivity. However, it is sufficient when this conductivity occurs within a single grain. A macroscopic conductivity or a conductivity across grain boundaries cannot be concluded from the voltammetric data for these films. In operando infrared reflection–absorption studies had shown that these films contain fewer defects at the molecular level than electrodeposited films.[41] These findings correspond to the results of XRD studies of the film shown in Figure 3. Well defined diffraction peaks are obtained from the film. A comparison with powder XRD data of CuHCF[39] reveals a preferential orientation of the crystals within the CuHCF film. Characterization of the film conductivity on a Au substrate is problematic because the gold substrate may contribute to the measured lateral conductivity. It is also extremely difficult to rule out the option of conductive shunts in through film conductivity measurements when connecting the films by evaporating materials on top of the film or mechanically contacting the film from the top.

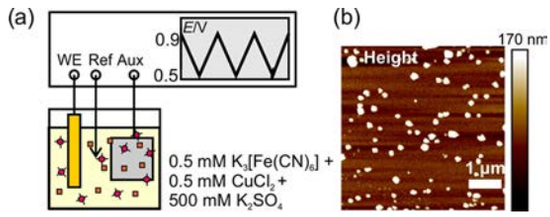

Figure 1. Schematics of (a) electrodeposition of CuHCF and (b) scanning force microscopy (SFM) contact mode images of electrodeposited CuHCF on Au. The scale bar in (b) is 1 μm.

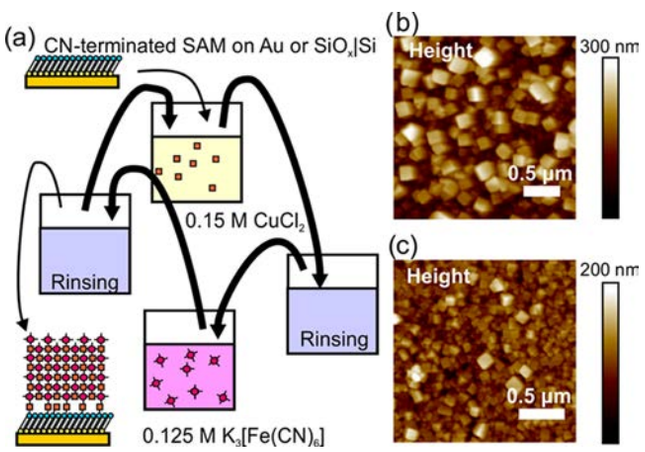

Figure 2. Schematics of (a) LbL deposition on the CN terminated self assembled monolayer (SAM) on Au or SiO_x|Si; SFM contact mode images of CuHCF from LbL on cyanide terminated self assembled monolayer on (b) Au and (c) SiO_x|Si. Scale bars in (b) and (c) are 0.5 μm.

Therefore, we carried out LbL deposition on a CN terminated organic layer on a SiO_x|Si wafer (Figure 2a). SFM images of the resulting film in Figure 2c show fewer well defined crystals than for LbL deposition on a CN terminated SAM on gold despite a comparable very small roughness of both substrates (Table 1). The crystals have a size of about 76 nm. No preferential orientation of the crystals can be identified from the SFM images in Figure 2c. The Fe/Cu stoichiometries in the film agree with that of the original powder within the uncertainty margins of XPS (Table S7). A higher C content in the films may result from adsorption of contaminations as well as from emissions from the exposed SAM in between crystals. The conductivity of the deposited thin films was too low to allow reproducible measurements of sheet conductivity probably caused by large contact resistance at the contact pads. This contact resistance could not be decreased by the applied force due to the low mechanical strength of this porous film.

Sonication-Assisted Casting. The contacting problem described above occurs commonly when MHCMs or other coordination network compounds such as metal–organic framework (MOF) compounds will be used as conductive

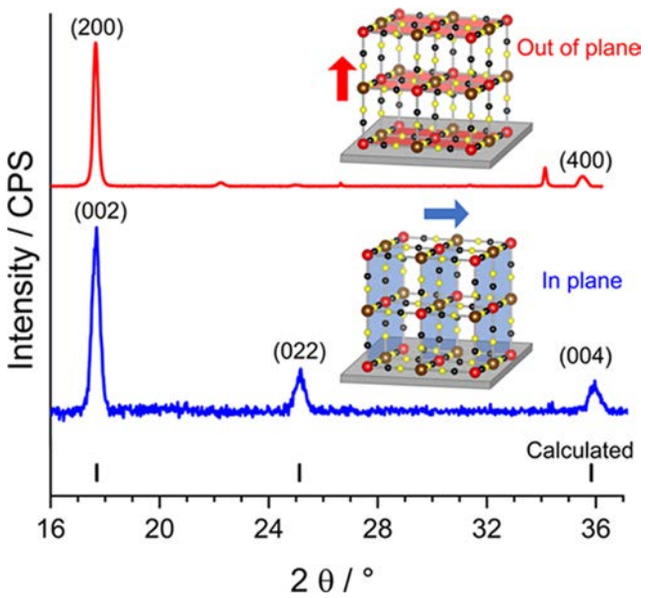

Figure 3. XRD pattern of CuHCF films obtained by LbL on a cyanide terminated self assembled monolayer on Au.

Table 1. Thicknesses of CuHCF Films Obtained from the LBL Procedure and Measured by SFM

item	LbL cycles	crystal size av. (nm)	roughness (nm)
LbL on Au	60	150 ± 30	45
LbL on SiO_x|Si	60	76 ± 14	19

layers in device applications. An obvious solution would be a coating method that, unlike the procedures in Figures 1 and 2, provides crystalline films independently on the used substrate materials. This would allow us to coat planar insulating chips with embedded contact electrodes with a film of uniform morphology and film properties. Along this line, Ono et al.[34] demonstrated the formation of a Prussian blue film between gold contact pads on a glass substrate coated with a monolayer of aminopropyl trimethoxy silane. Our approach is based on first synthesizing CuHCF (and in a similar way as for other MHCMs) in a bulk procedure, then casting this material as a film, and postprocessing the film to enhance the conductivity between the crystals that were already obtained in the bulk synthesis. There is no need for an organic interface layer on the substrate. The bulk synthesis can be described as

$$2x/3K^{+}_{(aq)} + Cu^{2+}_{(aq)} + 2/3[Fe^{III}(CN)_6]^{3-}_{(aq)} \rightarrow K_{2x/3}Cu^{II}[Fe^{III}(CN)_6]_{2/3}\cdot nH_2O_{(s)} \quad (4)$$

The stoichiometry of the products was verified by XPS and shows a K content of $x = 0.2$ (Table S7). The water content was determined by TGA with $n = 3.5$ (vide infra). Le Bail refinements in the *Fm*3*m* space group for XRD of the powder XRD samples (Figure S11) are in good agreement with reported structures.[39] Additional reflexes can be assigned by the lower symmetric *Pm*3*m* space group, which has been reported before for CuHCF.[39,60] The defects are isolated as indicated by the broadening and low intensity of the reflexes. Additional reflexes cannot be assigned. The respective data are shown in full detail in Section SI 4.

This product was then used for different variations of film casting procedures. Simple drop casting yielded films with

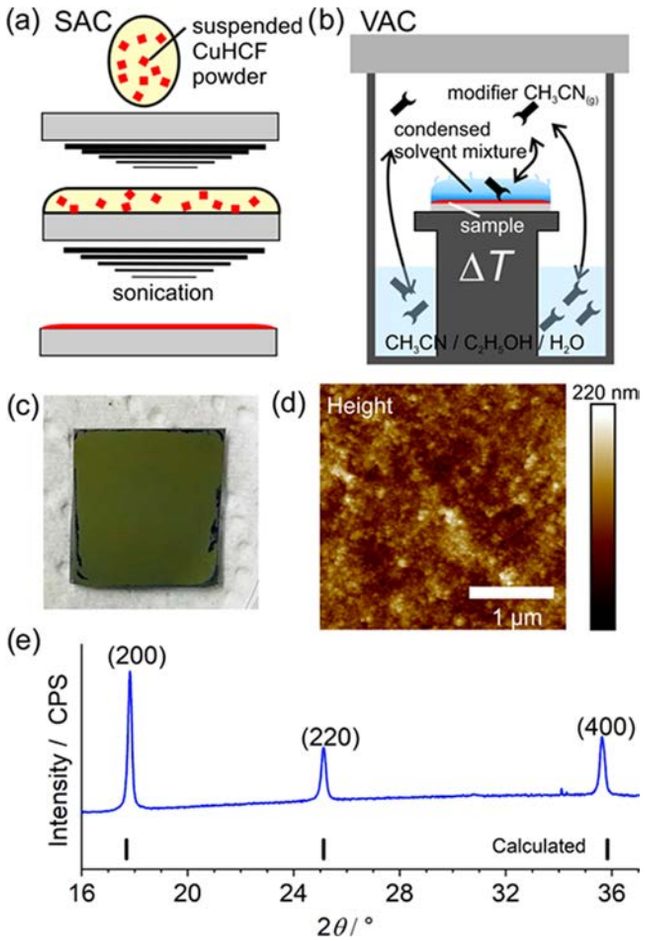

Figure 4. (a) Schematic representation of the SAC method, (b) VAC of the film from (a), (c) optical photograph of the film, (d) SFM contact image of the film prepared by SAC–VAC, and (e) XRD data of the film prepared by SAC–VAC.

strong coffee ring effects[61] unsuitable for film conductivity studies. Spin coating tended to give films that appeared macroscopically homogeneous but showed isolated crystals in SFM images. The first significant improvement was obtained by placing the SiO_x|Si substrate on a Petri dish that was floating in an ultrasound bath before drop casting a suspension of bulk synthesized CuHCF dispersed in an ethanol–water mixture [50/50% (v/v)]. For brevity, we call this procedure sonication assisted casting (SAC, Figure 4a). SAC efficiently suppressed the coffee ring effect and produced films of rather uniform and adjustable thicknesses. The minimum thickness is determined by the size of the crystals in the suspension. The maximum thickness is flexible and controlled by the applied amount of solid fraction per geometric surface area of the substrate. However, the conductivities of the films were too low for a reliable characterization in the dry state. We attribute this to the high resistance between the nanometer sized grains obtained in the bulk synthesis rather than to the intrinsic properties of CuHCF.

Vapor-Assisted Conversion. To improve the electrical contact between the crystallites in the casted film, we combined the SAC method with vapor assisted conversion (VAC) recently described for various inorganic films.[50−52,62] In this method, a weak monodentate ligand, acetonitrile in our case, is supplied via the gas phase and aids in solubilization–

redeposition processes in the defect rich outer regions of the initial crystals. While the application of the colloidal solution by the SAC method provides for a crack free and continuous film of small nuclei or crystals, the VAC step adds another secondary growth step, during which the initially weak particle−particle contacts are improved. The SFM image in Figure 4d and XRD data (Figure 4e) of the film did not show significant differences in the films obtained from SAC because these techniques mainly respond to the structures formed in the bulk synthesis. Individual crystals could not be recognized from SFM images, such as in Figure 4d. The XRD analysis of the film (Figure 4e) shows the same signals as for the product of the bulk synthesis (Figure S11), proving the crystallinity of the films. The much thicker films from the SAC−VAC procedure do not have a preferential orientation of the grains, which is in contrast to the films obtained from LbL deposition (cf. Figure 3). However, measurements of film conductivity were possible, and the values obtained are listed in Table 2.

Table 2. Thin Film Electrical Conductivity for Films Obtained by the SAC/VAC Method

compound	$\log(\sigma/\mathrm{S\ cm^{-1}})$
$Cu^{II}[Fe^{III}(CN)_6]_{2/3}\ nH_2O$, sample 1	2.4 ± 0.3
$Cu^{II}[Fe^{III}(CN)_6]_{2/3}\ nH_2O$, sample 2	1.1 ± 0.2
$Cu^{II}[Fe^{III}(CN)_6]_{2/3}\ nH_2O$, sample 3	2.0 ± 0.2
average of three samples	1.8 ± 0.7

The uncertainty of the conductivity for each sample is given as the standard deviation between 18 measurements of one film, while the uncertainty of the average is given as the standard deviation between the mean values of the three samples. The average conductivity of the three samples yielded a value of $\sigma = 1.58 \times 10^{-2}$ S cm^{-1}. Despite this high conductivity, the contact resistance between the CuHCF films and external contacts was too high and prevented reliable and repeatable Hall measure ments at a magnetic field of 0.55 T.

We attribute this conductivity of CuHCF films to a mixed electronic and ionic conductivity (including proton con ductivity). This conclusion is based on the recording of well defined signals in cyclic voltammograms of a 1 μm thick CuHCF film produced by the SAC−VAC method on a bare Au substrate without any conductivity additives and analyzed in 0.5 M K_2SO_4 solution at scan rates ν of 0.1, 1, and 50 mV s^{-1} (Figure 5). The electrochemical process is

$$K_2Cu_3^{(II)}[Fe^{(II)}(CN)_6]_2 = Cu_3^{(II)}[Fe^{(III)}(CN)_6]_2 + 2e^- + 2K^+ \quad (5)$$

The normalization of the plot with respect to ν allowed us to print all curves in the same diagram. Furthermore, the shaded areas under the current−voltage curve are directly proportional to the transferred charge.

$$Q = \frac{1}{A\nu}\int_{E_1}^{E_2} I(E)\,\mathrm{d}E \quad (6)$$

The voltammogram at ν = 0.1 mV s^{-1} was almost symmetrical with vanishing peak splitting $\Delta E_p = E_{p,a} - E_{p,c}$ between the anodic ($E_{p,a}$) and the cathodic ($E_{p,c}$) peak potentials (Table 3). This indicates an almost ideal reversible thin layer voltammetry, which can only be achieved when the transport processes are so fast with respect to the time scale of the experiment that no significant concentration gradient forms in the CuHCF film.

Table 3. Voltammetric Characteristics of a CuHCF Film Obtained by the SAC−VAC Method with a Thickness of 1 μm (Figure 5)

ν/mV s^{-1}	E_{pa}/V	E_{pc}/V	ΔE_p/V	Q/As cm^{-2}
0.1	0.767	0.753	0.014	0.147
1	0.786	0.763	0.023	0.119
50	0.915	0.679	0.236	0.108

These films have a thickness of 1 μm so that a complete conversion of the redox centers is possible only when electrons from the entire film can reach the Au contact electrode and the charge is compensated by the ingress/ejection of potassium ions. This requires the transport of electrons and alkali cations, i.e., mixed conductivity. This is remarkable for a film of this thickness produced without conductive additives.

The reversible character was lost gradually when higher scan rates were applied. However, the charge extracted from the film decreased only slightly (Table 3). It should be noted that the films obtained by electrodeposition and by LbL deposition, which are discussed in Figures 1−3, are much thinner than the SAC−VAC film investigated in Figure 5.

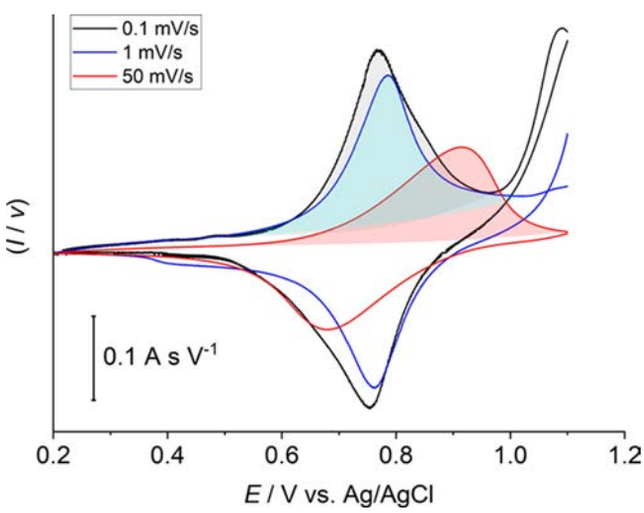

Figure 5. Cyclic voltammogram of a CuHCF film on an Au electrode (A = 0.217 cm^2) in 0.5 M K_2SO_4 solution at scan rates of 0.1, 1, and 50 mV s^{-1}. The plot is normalized to the scan rate.

Detailed Analysis of the Conductivity Mechanisms. For the analysis of the conductivity mechanisms, we used the bulk synthesized CuHCF powder and processed it to pellets, which allowed the characterization of conductivity by EIS. Despite the effect of grain boundaries in such pellets, the trends observed with the variation in temperature and relative humidity (RH) provide information about the intrinsic conduction mechanisms within grains of $Cu^{II}[Fe^{III}(CN)_6]_{2/3}\cdot nH_2O$. Figure 6 shows the product of conductivity and temperature σT in the temperature range between 20 and 120 °C for RH of 0 and 90%. The conductivity values and the complete EIS data are shown in Section SI 3. Between room temperature and 80 °C, σT depends linearly on the reciprocal temperature. Activation energies of 0.27 eV for dry atmosphere and 0.37 eV for 90% RH can be obtained from the slope.

These values are similar to the reported values of 0.48 eV for $Co^{II}[Cr^{III}(CN)_6]_{2/3}\cdot nH_2O$ and 0.36 eV for $Mn^{II}[Cr^{III}(CN)_6]_{2/3}\cdot nH_2O$.[35] The conductivity drops by approximately a factor of 30 from 5.5×10^{-7} S cm^{-1} at 100 °C to 1.9×10^{-8} S cm^{-1} at 120 °C (Figure S10).

It is generally accepted that proton conductivity significantly contributes to the conductivity of MHCMs by a Grotthuss mechanism that is enabled by an extended hydrogen bonding network between coordinated and zeolitic water present in MHCM structures.[34−36] The conductivity decrease above 100 °C in Figure 6 might be caused by the loss of water and concomitant interruption of the hydrogen bonding network required for efficient proton conductivity. Furthermore, it was shown before that proton conductivity of a Prussian blue film decreased in a D_2O atmosphere, again indicating the role of protons as charge carriers.[34] The activation energies in Figure 6 of 0.27 eV (dry atmosphere) and 0.37 eV (90% RH) are in agreement with proton hopping as the dominant conduction mechanism. Activation energies between 0.1 and 0.4 eV have been reported before for different water mediated proton conductors such as coordination polymers[63] or Nafion.[64] Proton hopping requires an extended hydrogen bonding network.[65] Potassium ions as possible alternative ionic charge carriers in $Cu^{II}[Fe^{III}(CN)_6]_{2/3}\cdot nH_2O$ cannot provide a conduction pathway of such low activation energy due to restrictions by the required space and charge neutrality.

Thermogravimetric analysis (Figure 7b,c) shows a gradual loss of water in the temperature range of 70−140 °C. Lattice constants (Figure 7a) extracted by Le Bail (Figures S11−S16) refinements from the temperature dependent XRD data in Figure 6b confirm the integrity of the structure, even the lattice constant remains constant until 80 °C despite the loss of water. Further fitting results are summarized in Table S7. We conclude that water lost below 80 °C is mainly zeolitic water, which can be released without affecting the crystal structure. This observation is also in agreement with previous reports for $Cu^{II}[Fe^{III}(CN)_6]_{2/3}\cdot nH_2O$ in the temperature range up to 120 °C.[39] The conductivity data do not seem to be affected by the loss of loosely bound zeolitic water, indicating that it is does not play a major role in the conduction mechanisms of CuHCF.

Above 80 °C, the lattice contracts (Figure 7a) and the reflexes broaden, in agreement with an incipient amorphization of the sample, which reaches its full extent at 120 °C, at which the conductivity also sharply decreases.[39,60] This is likely caused by the loss of coordinated water that is associated with missing transition metal ions in the cubic lattice (Scheme 1, right panel).

When cooling down the sample from 120 to 20 °C, the conductivity remains below the initial conductivity by a factor of 30 because the dry atmosphere does not provide enough water to resupply the water lost at temperatures above 100 °C. However, storing the sample for 3 h at 40 °C and 90% RH restored the initial conductivity, while the crystal structure is only partially restored (Figure S17). The conductivity values determined at 90% RH are slightly above the values determined in a nonhumidified atmosphere (Figure 6a). However, the activation energy increased from 0.27 to 0.37 eV since the slightly impaired structure after heating to 120 °C causes a more disordered hydrogen bonding network in which the proton hopping is less effective than that in pristine CuHCF. This is in contrast to films of PB nanoparticles, whose surface had partially been modified with $[Fe(CN)_6]^{4-}$ and the grain boundaries vanished upon heating to 120 °C, which in turn facilitated effective grain boundary free proton hopping with low activation energies.[34]

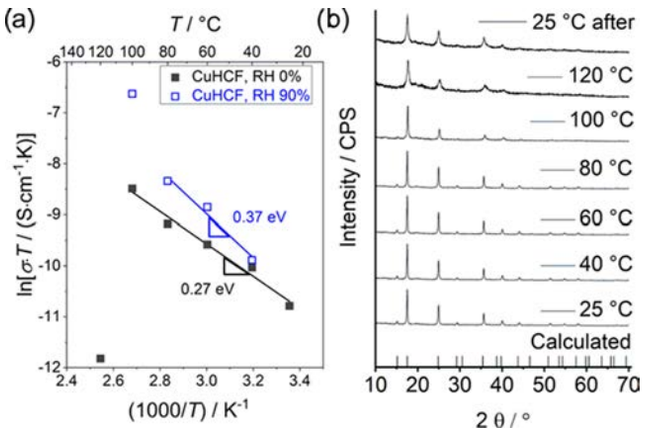

Figure 6. Temperature dependent conductivity data (a) for CuHCF pellets at a dry atmosphere (■) and at 90% relative humidity (RH) (□). Lines are linear fits from which the activation energy is obtained as well as temperature dependent XRD data (b) from the powder sample in a nonhumidified atmosphere, i.e., at ambient conditions.

To verify that indeed the VAC treatment dramatically improves the conductivity in measurements outside an

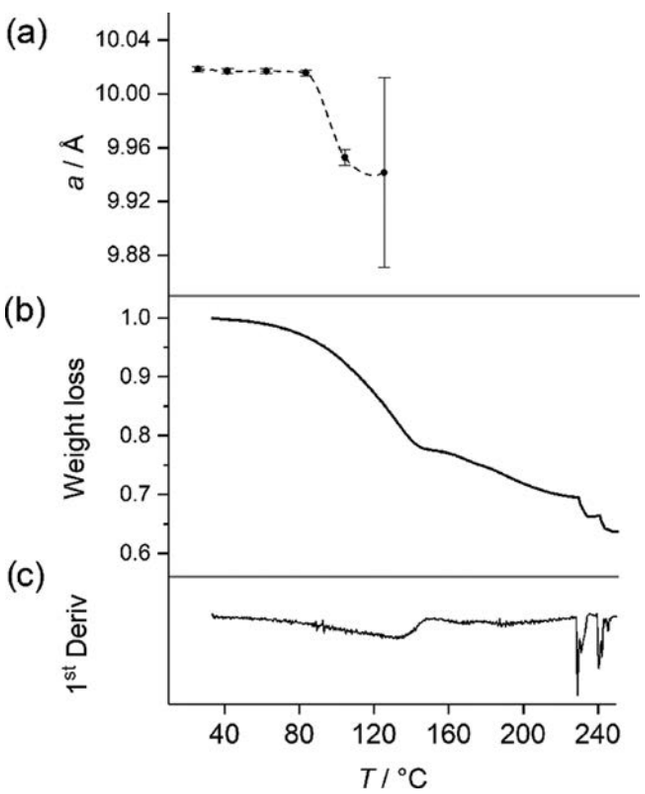

Figure 7. Temperature dependent structural changes of $K_{2x/3}Cu^{II}[Fe^{III}(CN)_6]_{2/3}\cdot nH_2O$. (a) Change of lattice parameter *a* obtained from Le Bail refinements of the XRD data (Figures S11−S16); error bars are uncertainty ranges of the refinement. (b) TGA and the (c) differential thermal analysis (DTA) curves. The sample was equilibrated at 30 °C and heated at 10 °C min^{-1} to 250 °C in ambient conditions.

electrolyte solution, we first characterized a fresh powder pellet by EIS, yielding the Nyquist plot in Figure 8, curve 1. Then, the pellet was subjected to VAC treatment while it remained sandwiched between the porous current collectors. To mitigate the larger sample thickness and the presence of the porous current collectors during VAC treatment, we used a 12 h VAC treatment for the pellet instead of 3 h for the 1 μm uncovered film studied in Table 2.

The VAC treated pellet was again connected to the EIS workstation. The Nyquist plot in Figure 8, curve 2, shows a strongly reduced resistance of the VAC treated sample. The full details are only appreciable when curve 2 is shown on an expanded scale in the inset of Figure 8. The VAC treatment increased the conductivity of the CuHCF pellet by one order of magnitude from 7.43×10^{-8} to 7.91×10^{-7} S cm^{-1}. Furthermore, some mechanistic insights can be deduced. The pristine sample in Figure 8, curve 1, gave a depressed semicircle with a crumbled tail in the Nyquist plot. The high frequency intercept represents the bulk resistance used to calculate the proton conductivity. The tail of the Nyquist plot accounts for diffusion processes. The degree to which a tail develops in the Nyquist plot correlates with the diffusion coefficient of the involved species.[66] A high bulk resistance along with a poorly developed tail in the Nyquist plot of a coordination polymer was previously associated with low proton conductivity due to reduced water mobility.[67]

The comparison of the Nyquist plots of the pristine sample and the VAC treated sample in Figure 8 revealed a strong decrease of the bulk polarization of the sample. Before the treatment, the tail in the Nyquist plot (curve 1 of Figure 8) is poorly developed, indicating low mobility of water. The fully developed tail in curve 2 of Figure 8 (well visible in the inset) points toward an increased mobility of water and the associated proton conductivity by a Grotthuss mechanism. The same finding was reported for nanoparticulate PB films in which the grain boundaries were healed by temperature treatment. The Nyquist plot of the untreated particle film revealed a crumbled tail, while the temperature treated film gave a distinctly developed tail.[34]

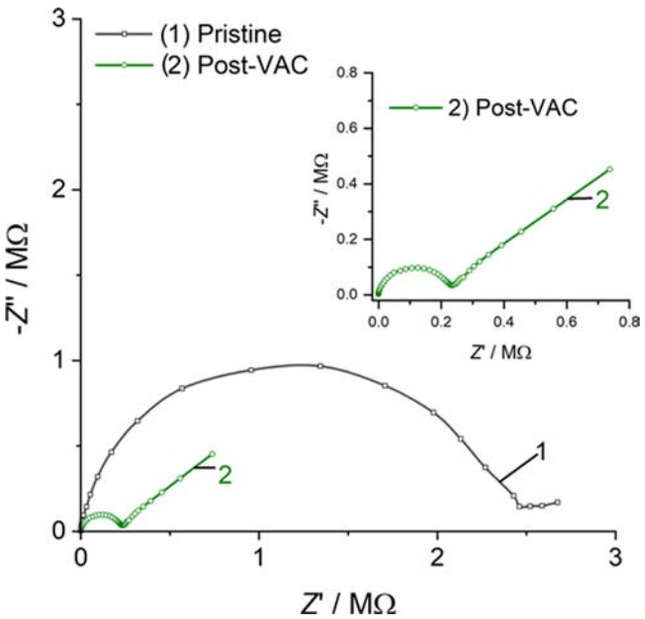

Figure 8. EIS data between 1 Hz and 1 MHz of a $K_{2x/3}Cu^{II}[Fe^{III}(CN)_6]_{2/3}\cdot nH_2O$ powder pellet at room temperature in a dry atmosphere (1) before and (2) after VAC treatment. The inset shows curve 2 on an expanded scale.

CONCLUSIONS

This work demonstrates for copper hexacyanoferrate that the electrical conductivity of coordination network compounds may decisively depend on the way the material is processed. We succeeded to devise a simple method for preparation of conducting films of metal hexacyanoferrates without the need for surface pretreatment. This is especially helpful when coating substrates are composed of different materials. For this purpose, copper hexacyanoferrate was obtained by mixing precursors in solution. The obtained suspension was then cast during sonication on the substrate. Subsequent vapor assisted conversion improved the contact between the particles in the film. Films obtained in this way showed electrical conductivities of 1.58×10^{-2} S cm^{-1} without the addition of conductive additives, which is orders of magnitude higher than the film conductivity of powder pellets of the same material. The conductivity is also better than that in films obtained by layer by layer deposition with a preferential orientation of crystal planes but insufficient contact between the grains. Cyclic voltammograms of films prepared by the SAC–VAC method showed reversible thin film voltammetry, indicating a mixed electronic and ionic conductivity. Temperature dependent and humidity dependent conductivity data, thermogravimetric analysis data, and temperature dependent XRD data of powder pellets confirmed the critical role of water that is removed gradually from the structure until 140 °C. The loss of water occurs up to 80 °C without any change in the lattice constant, while above 80 °C, the crystal contracts and the crystallinity decreases. Upon cooling samples, the conductivity can be fully recovered, while the crystallinity can only be partially restored. The VAC treatment of powder pellets resulted in an enhanced conductivity as it was also found for films.

AUTHOR INFORMATION

Corresponding Author

Gunther Wittstock – *Department of Chemistry, Carl von Ossietzky University of Oldenburg, 26129 Oldenburg, Germany;* orcid.org/0000 0002 6884 5515; Email: wittstock@uol.de

Authors

Pouya Hosseini – *Department of Chemistry, Carl von Ossietzky University of Oldenburg, 26129 Oldenburg, Germany;* orcid.org/0000 0003 4492 0004

Konrad Wolkersdörfer – *Department of Chemistry, Carl von Ossietzky University of Oldenburg, 26129 Oldenburg, Germany*

Michael Wark − *Department of Chemistry, Carl von Ossietzky University of Oldenburg, 26129 Oldenburg, Germany;* orcid.org/0000 0002 8725 0103

Engelbert Redel − *Institute of Functional Interfaces (IFG), Karlsruhe Institute of Technology, 76344 Eggenstein Leopoldshafen, Germany*

Helmut Baumgart − *Department of Electrical and Computer Engineering, Old Dominion University, Norfolk, Virginia 23529, United States; Applied Research Center, Newport News, Virginia 23606, United States*

Author Contributions

P.H. conducted the synthesis of CuHCF, the preparation of the substrates by different methods, as well as their characterization by SFM, voltammetry, and XPS. K.W. and M.W. performed proton conductivity, XRD, and TGA measurements as well as the corresponding data analysis. E.R. prepared the oxide coated substrates and performed in plane and out of plane XRD measurements. P.H. and K.W. fitted the XRD data. H.B. conducted the electrical conductivity σ measurements on chips. G.W. conceived the project idea and coordinated the work. The manuscript was written through the contribution of all authors. All authors have given approval to the final version of the manuscript.

Notes

The authors declare no competing financial interest.

ACKNOWLEDGMENTS

The research was funded by Deutsche Forschungsgemeinschaft within the Priority Program SPP 1928 "Coordination Net works: Building Blocks for Functional Systems" (Wi1617/24, Wa1116/30 1, Re3044/5, and a Mercator fellowship to H.B.). E. R. thanks KIT and CMM for sustainable research funding. The XPS and XRD instrumentation were cofunded by the German Research Foundation (DFG) through grants INST 184/144 1 FUGG and INST 184/154 1 FUGG, respectively.

ABBREVIATIONS

CuHCF, copper hexacyanoferrate; CoHCF, cobalt hexacyano ferrate; IR, infrared; LbL, layer by layer; MHCM, metal hexacyanometalate; MOF, metal−organic framework; RH, relative humidity; SAC, sonication assisted casting; SAM, self assembled monolayer; SFM, scanning force microscopy; TGA, thermogravimetric analysis; VAC, vapor assisted casting; XPS, X ray photoelectron spectroscopy; XRD, X ray diffraction

REFERENCES

(1) de Tacconi, N. R.; Rajeshwar, K.; Lezna, R. O. Metal Hexacyanoferrates: Electrosynthesis, in Situ Characterization, and Applications. *Chem. Mater.* **2003**, *15*, 3046−3062.

(2) Paolella, A.; Faure, C.; Timoshevskii, V.; Marras, S.; Bertoni, G.; Guerfi, A.; Vijh, A.; Armand, M.; Zaghib, K. A Review on Hexacyanoferrate based Materials for Energy Storage and Smart Windows: Challenges and Perspectives. *J. Mater. Chem. A* **2017**, *5*, 18919−18932.

(3) Zakaria, M. B.; Chikyow, T. Recent Advances in Prussian Blue and Prussian Blue Analogues: Synthesis and Thermal Treatments. *Coord. Chem. Rev.* **2017**, *352*, 328−345.

(4) Keggin, J. F.; Miles, F. D. Structures and Formulae of the Prussian Blues and Related Compounds. *Nature* **1936**, *137*, 577−578.

(5) Kraft, A. What a Chemistry Student Should Know about the History of Prussian Blue. *ChemTexts* **2018**, *4*, No. 16.

(6) Frisch, J. L. F. Notitia Coerulei Berolinensis. *Miscnea Berol. Soc. Sci.* **1710**, 377−379.

(7) Widmann, A.; Kahlert, H.; Petrovic Prelevic, I.; Wulff, H.; Yakhmi, J. V.; Bagkar, N.; Scholz, F. Structure, Insertion Electro chemistry, and Magnetic Properties of a New Type of Substitutional Solid Solutions of Copper, Nickel, and Iron Hexacyanoferrates/ Hexacyanocobaltates. *Inorg. Chem.* **2002**, *41*, 5706−5715.

(8) Brown, D. B.; Shriver, D. F. Structures and Solid State Reactions of Prussian Blue Analogs Containing Chromium, Manganese, Iron, and Cobalt. *Inorg. Chem.* **1969**, *8*, 37−42.

(9) Weiser, H. B.; Milligan, W. O.; Bates, J. B. X ray Diffraction Studies on Heavy Metal Iron Cyanides. *J. Phys. Chem. A.* **1942**, *46*, 99−111.

(10) Ludi, A. Berliner Blau. *Chem. Unserer Zeit* **1988**, *22*, 123−127.

(11) Kaye, S. S.; Long, J. R. Hydrogen Storage in the Dehydrated Prussian Blue Analogues $M_3[Co(CN)_6]_2$ (M = Mn, Fe, Co, Ni, Cu, Zn). *J. Am. Chem. Soc.* **2005**, *127*, 6506−6507.

(12) Itaya, K.; Uchida, I.; Neff, V. D. Electrochemistry of Polynuclear Transition Metal Cyanides: Prussian Blue and Its Analogues. *Acc. Chem. Res.* **1986**, *19*, 162−168.

(13) Karyakin, A. A. Prussian Blue and Its Analogues: Electro chemistry and Analytical Applications. *Electroanalysis* **2001**, *13*, 813−819.

(14) Narayanan, S. S.; Scholz, F. A Comparative Study of the Electrocatalytic Activities of Some Metal Hexacyanoferrates for the Oxidation of Hydrazine. *Electroanalysis* **1999**, *11*, 465−469.

(15) Yi, I. J.; Kim, J. H.; Kang, C. J.; Choi, Y. J.; Lee, K.; Kim, Y. S. A Novel Electrochemical Detector using Prussian Blue Modified Indium Tin Oxide Electrode. *Jpn. J. Appl. Phys.* **2006**, *45*, 438−441.

(16) Düssel, H.; Dostal, A.; Scholz, F. Hexacyanoferrate Based Composite Ion Sensitive Electrodes for Voltammetry. *Fresenius' J. Anal. Chem.* **1996**, *355*, 21−28.

(17) Nigrović, V. Enhancement of the Excretion of Radiocaesium in Rats by Ferric Cyanoferrate (II). *Int. J. Radiat. Biol. Relat. Stud. Phys., Chem. Med.* **1963**, *7*, 307−309.

(18) Clarke, T. D.; Wai, C. M. Selective Removal of Cesium from Acid Solutions with Immobilized Copper Ferrocyanide. *Anal. Chem.* **1998**, *70*, 3708−3711.

(19) Parajuli, D.; Kitajima, A.; Takahashi, A.; Tanaka, H.; Ogawa, H.; Hakuta, Y.; Yoshino, K.; Funahashi, T.; Yamaguchi, M.; Osada, M.; Kawamoto, T. Application of Prussian Blue Nanoparticles for the Radioactive Cs Decontamination in Fukushima Region. *J. Environ. Radioact.* **2016**, *151*, 233−237.

(20) Liu, J.; Zhou, W.; Walheim, S.; Wang, Z.; Lindemann, P.; Heissler, S.; Liu, J.; Weidler, P. G.; Schimmel, T.; Wöll, C.; Redel, E. Electrochromic Switching of Monolithic Prussian Blue Thin Film Devices. *Opt. Express* **2015**, *23*, 13725−13733.

(21) DeLongchamp, D. M.; Hammond, P. T. High Contrast Electrochromism and Controllable Dissolution of Assembled Prussian Blue/Polymer Nanocomposites. *Adv. Funct. Mater.* **2004**, *14*, 224−232.

(22) Wessells, C. D.; Huggins, R. A.; Cui, Y. Copper Hexacyanoferrate Battery Electrodes with Long Cycle Life and High Power. *Nat. Commun.* **2011**, *2*, No. 550.

(23) Wang, B.; Han, Y.; Wang, X.; Bahlawane, N.; Pan, H.; Yan, M.; Jiang, Y. Prussian Blue Analogs for Rechargeable Batteries. *iScience* **2018**, *3*, 110−133.

(24) Li, W. J.; Han, C.; Cheng, G.; Chou, S. L.; Liu, H. K.; Dou, S. X. Chemical Properties, Structural Properties, and Energy Storage Applications of Prussian Blue Analogues. *Small* **2019**, *15*, No. 1900470.

(25) Neff, V. D. Some Performance Characteristics of a Prussian Blue Battery. *J. Electrochem. Soc.* **1985**, *132*, 1382−1384.

(26) Paulitsch, B.; Yun, J.; Bandarenka, A. S. Electrodeposited $Na_2VO_xFe(CN)_6$ Films as a Cathode Material for Aqueous Na Ion Batteries. *ACS Appl. Mater. Interfaces* **2017**, *9*, 8107−8112.

(27) Sun, L.; Campbell, M. G.; Dinca, M. Electrically Conductive Porous Metal Organic Frameworks. *Angew. Chem., Int. Ed.* **2016**, *55*, 3566−3579.
(28) Wojdeł, J. C.; Moreira, I. d. P. R.; Bromley, S. T.; Illas, F. Prediction of Half Metallic Conductivity in Prussian Blue Derivatives. *J. Mater. Chem.* **2009**, *19*, 2032−2036.
(29) Kulesza, P. J.; Galus, Z. Mixed Valence Electron Hopping, Redox Conduction and Migration Effects in Solid State Electro chemistry of Transition Metal Hexacyanoferrates. *J. Electroanal. Chem.* **1992**, *323*, 261−274.
(30) Manumpil, M. A.; Leal Cervantes, C.; Hudson, M. R.; Brown, C. M.; Karunadasa, H. I. Electronic Conductivity in a Porous Vanadyl Prussian Blue Analogue upon Air Exposure. *Inorg. Chem.* **2017**, *56*, 12682−12686.
(31) Behera, J. N.; D'Alessandro, D. M.; Soheilnia, N.; Long, J. R. Synthesis and Characterization of Ruthenium and Iron−Ruthenium Prussian Blue Analogues. *Chem. Mater.* **2009**, *21*, 1922−1926.
(32) Rosseinsky, D. R.; Tonge, J. S.; Berthelot, J.; Cassidy, J. F. Site Transfer Conductivity in Solid Iron Hexacyanoferrates by Dielectric Relaxometry, Voltammetry and Spectroscopy. Prussian Blue, Con geners and Mixtures. *J. Chem. Soc., Faraday Trans. 1* **1987**, *83*, 231−243.
(33) Ishizaki, M.; Ando, H.; Yamada, N.; Tsumoto, K.; Ono, K.; Sutoh, H.; Nakamura, T.; Nakao, Y.; Kurihara, M. Redox Coupled Alkali Metal Ion Transport Mechanism in Binder Free Films of Prussian Blue Nanoparticles. *J. Mater. Chem. A* **2019**, *7*, 4777−4787.
(34) Ono, K.; Ishizaki, M.; Kanaizuka, K.; Togashi, T.; Yamada, T.; Kitagawa, H.; Kurihara, M. Grain Boundary Free Super Proton Conduction of a Solution Processed Prussian Blue Nanoparticle Film. *Angew. Chem., Int. Ed.* **2017**, *56*, 5531−5535.
(35) Ohkoshi, S. i.; Nakagawa, K.; Tomono, K.; Imoto, K.; Tsunobuchi, Y.; Tokoro, H. High Proton Conductivity in Prussian Blue Analogues and the Interference Effect by Magnetic Ordering. *J. Am. Chem. Soc.* **2010**, *132*, 6620−6621.
(36) Wu, X.; Hong, J. J.; Shin, W.; Ma, L.; Liu, T.; Bi, X.; Yuan, Y.; Qi, Y.; Surta, T. W.; Huang, W.; Neuefeind, J.; Wu, T.; Greaney, P. A.; Lu, J.; Ji, X. Diffusion Free Grotthuss Topochemistry for High Rate and Long Life Proton Batteries. *Nat. Energy* **2019**, *4*, 123−130.
(37) Sequeda, F. The Role of Thin Film Materials on the Technology of Integrated Circuit Fabrication. *JOM* **1985**, *37*, 54−60.
(38) Momma, K.; Izumi, F. VESTA 3 for Three Dimensional Visualization of Crystal, Volumetric and Morphology Data. *J. Appl. Crystallogr.* **2011**, *44*, 1272−1276.
(39) Ojwang, D. O.; Grins, J.; Wardecki, D.; Valvo, M.; Renman, V.; Häggström, L.; Ericsson, T.; Gustafsson, T.; Mahmoud, A.; Hermann, R. P.; Svensson, G. Structure Characterization and Properties of K Containing Copper Hexacyanoferrate. *Inorg. Chem.* **2016**, *55*, 5924−5934.
(40) Buser, H. J.; Schwarzenbach, D.; Petter, W.; Ludi, A. The Crystal Structure of Prussian Blue: $Fe_4[Fe(CN)_6]_3.xH_2O$. *Inorg. Chem.* **1977**, *16*, 2704−2710.
(41) Hosseini, P.; Wittstock, G.; Brand, I. Infrared Spectroelec trochemical Analysis of Potential Dependent Changes in Cobalt Hexacyanoferrate and Copper Hexacyanoferrate Flms on Gold Electrodes. *J. Electroanal. Chem.* **2018**, *812*, 199−206.
(42) Kulesza, P. J.; Malik, M. A.; Denca, A.; Strojek, J. In Situ FT IR/ATR Spectroelectrochemistry of Prussian Blue in the Solid State. *Anal. Chem.* **1996**, *68*, 2442−2446.
(43) Samain, L.; Grandjean, F.; Long, G. J.; Martinetto, P.; Bordet, P.; Strivay, D. Relationship between the Synthesis of Prussian Blue Pigments, Their Color, Physical Properties, and Their Behavior in Paint Layers. *J. Phys. Chem. C* **2013**, *117*, 9693−9712.
(44) Bonhommeau, S.; Pontius, N.; Cobo, S.; Salmon, L.; de Groot, F. M. F.; Molnár, G.; Bousseksou, A.; Dürr, H. A.; Eberhardt, W. Metal to Ligand and Ligand to Metal Charge Transfer in Thin Films of Prussian Blue Analogues Investigated by X ray Absorption Spectroscopy. *Phys. Chem. Chem. Phys.* **2008**, *10*, 5882−5889.
(45) Sauter, S.; Wittstock, G.; Szargan, R. Localisation of Electrochemical Oxidation Processes in Nickel and Cobalt Hex acyanoferrates investigated by Analysis of the Multiplet Patterns in X ray Photoelectron Spectra. *Phys. Chem. Chem. Phys.* **2001**, *3*, 562−569.
(46) Cano, A.; Rodríguez Hernández, J.; Reguera, L.; Rodríguez Castellón, E.; Reguera, E. On the Scope of XPS as Sensor in Coordination Chemistry of Transition Metal Hexacyanometallates. *Eur. J. Inorg. Chem.* **2019**, *2019*, 1724−1732.
(47) Verdaguer, M.; Bleuzen, A.; Marvaud, V.; Vaissermann, J.; Seuleiman, M.; Desplanches, C.; Scuiller, A.; Train, C.; Garde, R.; Gelly, G.; Lomenech, C.; Rosenman, I.; Veillet, P.; Cartier, C.; Villain, F. Molecules to Build Solids: High T_C Molecule Based Magnets by Design and Recent Revival of Cyano Complexes Chemistry. *Coord. Chem. Rev.* **1999**, *190−192*, 1023−1047.
(48) Hegner, F. S.; Galán Mascarós, J. R.; López, N. A Database of the Structural and Electronic Properties of Prussian Blue, Prussian White, and Berlin Green Compounds through Density Functional Theory. *Inorg. Chem.* **2016**, *55*, 12851−12862.
(49) Ayrault, S. Copper Hexacyanoferrates: Preparation, Composi tion and Structure. *Talanta* **1994**, *41*, 1435−1452.
(50) Virmani, E.; Rotter, J. M.; Mähringer, A.; von Zons, T.; Godt, A.; Bein, T.; Wuttke, S.; Medina, D. D. On Surface Synthesis of Highly Oriented Thin Metal Organic Framework Films through Vapor Assisted Conversion. *J. Am. Chem. Soc.* **2018**, *140*, 4812−4819.
(51) Rangnekar, N.; Mittal, N.; Elyassi, B.; Caro, J.; Tsapatsis, M. Zeolite Membranes A Review and Comparison with MOFs. *Chem. Soc. Rev.* **2015**, *44*, 7128−7154.
(52) Xu, W.; Dong, J.; Li, J.; Li, J.; Wu, F. A Novel Method for the Preparation of Zeolite ZSM 5. *J. Chem. Soc., Chem. Commun.* **1990**, 755−756.
(53) Rhauderwiek, T.; Wolkersdörfer, K.; Øien Ødegaard, S.; Lillerud, K. P.; Wark, M.; Stock, N. Crystalline and Permanently Porous Porphyrin Based Metal Tetraphosphonates. *Chem. Commun.* **2018**, *54*, 389−392.
(54) Feyand, M.; Seidler, C. F.; Deiter, C.; Rothkirch, A.; Lieb, A.; Wark, M.; Stock, N. High Throughput Microwave Assisted Discovery of New Metal Phosphonates. *Dalton Trans.* **2013**, *42*, 8761−8770.
(55) Wang, X.; Zhang, Y.; Jiang, S.; Ji, X.; Liu, Y.; Banks, C. E. Cubic Copper Hexacyanoferrates Nanoparticles: Facile Template Free Deposition and Electrocatalytic Sensing Towards Hydrazine. *Int. J. Electrochem.* **2011**, *2011*, No. 395724.
(56) Al Kutubi, H.; Gascon, J.; Sudhölter, E. J. R.; Rassaei, L. Electrosynthesis of Metal Organic Frameworks: Challenges and Opportunities. *ChemElectroChem* **2015**, *2*, 462−474.
(57) Campagnol, N.; van Assche, T. R. C.; Li, M.; Stappers, L.; Dincă, M.; Denayer, J. F. M.; Binnemans, K.; De Vos, D. E.; Fransaer, J. On the Electrochemical Deposition of Metal−Organic Frameworks. *J. Mater. Chem. A* **2016**, *4*, 3914−3925.
(58) Ventura, M.; Mullaliu, A.; Ciurduc, D. E.; Zappoli, S.; Giuli, G.; Tonti, D.; Enciso, E.; Giorgetti, M. Thin Layer Films of Copper Hexacyanoferrate: Structure Identification and Analytical Applica tions. *J. Electroanal. Chem.* **2018**, *827*, 10−20.
(59) Nakanishi, S.; Lu, G.; Kothari, H. M.; Bohannan, E. W.; Switzer, J. A. Epitaxial Electrodeposition of Prussian Blue Thin Films on Single Crystal Au(110). *J. Am. Chem. Soc.* **2003**, *125*, 14998−14999.
(60) Adak, S.; Daemen, L. L.; Hartl, M.; Williams, D.; Summerhill, J.; Nakotte, H. Thermal expansion in 3d metal Prussian Blue Analogs A survey study. *J. Solid State Chem.* **2011**, *184*, 2854−2861.
(61) Larson, R. G. Twenty Years of Drying Droplets. *Nature* **2017**, *550*, 466−467.
(62) Guerrero, V. V.; Yoo, Y.; McCarthy, M. C.; Jeong, H. K. HKUST 1 Membranes on Porous Supports Using Secondary Growth. *J. Mater. Chem.* **2010**, *20*, 3938−3943.
(63) Shigematsu, A.; Yamada, T.; Kitagawa, H. Wide Control of Proton Conductivity in Porous Coordination Polymers. *J. Am. Chem. Soc.* **2011**, *133*, 2034−2036.
(64) Kusoglu, A.; Weber, A. Z. New Insights into Perfluorinated Sulfonic Acid Ionomers. *Chem. Rev.* **2017**, *117*, 987−1104.

(65) Kreuer, K. D.; Paddison, S. J.; Spohr, E.; Schuster, M. Transport in Proton Conductors for Fuel Cell Applications: Simulations, Elementary Reactions, and Phenomenology. *Chem. Rev.* **2004**, *104*, 4637−4678.
(66) Walter, G. W. A Review of Impedance Plot Methods Used for Corrosion Performance Analysis of Painted Metals. *Corros. Sci.* **1986**, *26*, 681−703.
(67) Wang, S.; Wahiduzzaman, M.; Davis, L.; Tissot, A.; Shepard, W.; Marrot, J.; Martineau Corcos, C.; Hamdane, D.; Maurin, G.; Devautour Vinot, S.; Serre, C. A Robust Zirconium Amino Acid Metal Organic Framework for Proton Conduction. *Nat. Commun.* **2018**, *9*, No. 4937.